

OPEN

# Bulk and interfacial properties of decane in the presence of carbon dioxide, methane, and their mixture

Nilesh Choudhary, Arun Kumar Narayanan Nair\*, Mohd Fuad Anwari Che Ruslan &amp; Shuyu Sun\*

Molecular dynamics simulations were performed to study the bulk and interfacial properties of methane + n-decane, carbon dioxide + n-decane, and methane + carbon dioxide + n-decane systems under geological conditions. In addition, theoretical calculations using the predictive Peng-Robinson equation of state and density gradient theory are carried out to compare with the simulation data. A key finding is the preferential dissolution in the decane-rich phase and adsorption at the interface for carbon dioxide from the methane/carbon dioxide mixture. In general, both the gas solubility and the swelling factor increase with increasing pressure and decreasing temperature. Interestingly, the methane solubility and the swelling of the methane + n-decane system are not strongly influenced by temperature. Our results also show that the presence of methane increases the interfacial tension (IFT) of the carbon dioxide + n-decane system. Typically, the IFT of the studied systems decreases with increasing pressure and temperature. The relatively higher surface excess of the carbon dioxide + n-decane system results in a steeper decrease in its IFT as a function of pressure. Such systematic investigations may help to understand the behavior of the carbon dioxide-oil system in the presence of impurities such as methane for the design and operation of carbon capture and storage and enhanced oil recovery processes.

Since the beginning of the industrial revolution in the mid-1700s, driven by the burning of fossil fuels, there has been a steady increase in the emission of the greenhouse gas CO<sub>2</sub> into the atmosphere. According to recent reports, anthropogenic CO<sub>2</sub> emissions are more than 30 Gt per year, primarily from the combustion of fossil fuels<sup>1</sup>. Anthropogenic CO<sub>2</sub> emissions play an important role in global warming and the continued increase in the amount of CO<sub>2</sub> in the atmosphere is predicted to lead to significant environmental issues<sup>2–5</sup>. For example, oceans are becoming warmer and more acidic, and sea levels are rising rapidly as global warming melts glaciers and ice sheets. The Intergovernmental Panel on Climate Change projects a sea-level rise of 28–61 cm by 2100, if greenhouse gas emissions are significantly reduced<sup>4</sup>. At the Paris climate conference<sup>6</sup>, nearly 200 countries agreed to a target of keeping global warming below 2 °C above the pre-industrial average. In this context, carbon capture and storage (CCS) is considered to be a key technology for reducing anthropogenic CO<sub>2</sub> emissions. A variety of materials have been considered for CO<sub>2</sub> capture including metal-organic frameworks<sup>7–9</sup>, zeolites<sup>8,10</sup>, zeolitic imidazolate frameworks<sup>11</sup>, polymers<sup>10,12–14</sup>, and geological formations<sup>15–26</sup>. CCS will complement other crucial technologies, such as the use of renewable energy (solar, wind, etc.), increasing energy efficiency, and switching to low-carbon fuels.

Since many decades, enhanced oil recovery (EOR) techniques have been used in order to improve both oil field production and CO<sub>2</sub> sequestration<sup>19–26</sup>. In 2013, CO<sub>2</sub>-EOR provided about 4% (0.28 million barrels per day) of the total U.S. crude oil production and its contribution is projected to increase in the future<sup>26</sup>. Properties such as interfacial tension (IFT), density, miscibility, and solubility of the CO<sub>2</sub>-oil system are key for CO<sub>2</sub>-EOR. For example, a decrease in the IFT generally resulted in an increase in the oil yield of the CO<sub>2</sub> flooding process. Typically, the miscible CO<sub>2</sub> flooding process recovers 10–20% of the original oil in place (OOIP), whereas the immiscible CO<sub>2</sub> flooding process recovers 5–10% of the OOIP due to the interfacial tension between CO<sub>2</sub> and

Physical Science and Engineering Division (PSE), Computational Transport Phenomena Laboratory, King Abdullah University of Science and Technology (KAUST), Thuwal, 23955-6900, Saudi Arabia. \*email: [arun.narayanannair@kaust.edu.sa](mailto:arun.narayanannair@kaust.edu.sa); [shuyu.sun@kaust.edu.sa](mailto:shuyu.sun@kaust.edu.sa)

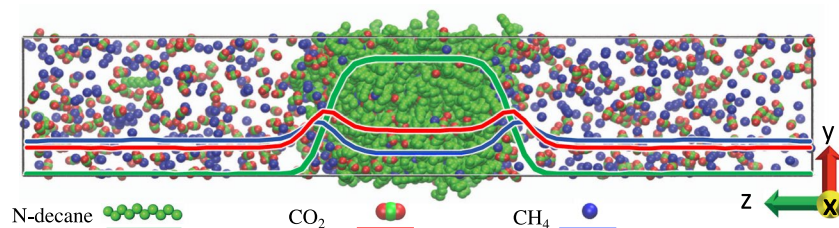


**Figure 1.** Equilibrium snapshot of the  $\text{CH}_4 + \text{CO}_2 + \text{n-decane}$  system at 343 K and 60 bar.

oil<sup>24</sup>. Traditionally, natural sources of  $\text{CO}_2$  are used for about 90% of EOR production in the U.S.<sup>23</sup>. However, EOR using anthropogenic  $\text{CO}_2$  emissions would be necessary to achieve the desired climate benefits.  $\text{CO}_2$  captured from power plants and industrial sources may contain impurities<sup>27–29</sup>. The cost of purification of gas mixtures considerably increases for obtaining a product of high degree of purity. Therefore, it is important to study the behavior of the  $\text{CO}_2$ -oil system in the presence of impurities such as methane for the design and operation of CCS and EOR processes.

The bulk and interfacial properties of binary mixtures of methane or carbon dioxide with alkanes such as n-decane (model oil in this work) under reservoir conditions receive continuous attention and many experimental<sup>30–42</sup>, theoretical<sup>38–41,43–51</sup>, and simulation<sup>39,46,52–56</sup> studies have been reported. These studies, for example, showed that the mole fractions of methane and carbon dioxide in the decane-rich phase increase with pressure. In general, the IFT of  $\text{CH}_4 + \text{n-decane}$  and  $\text{CO}_2 + \text{n-decane}$  systems decreases with increasing pressure and temperature. However, at high pressures, the IFT of the  $\text{CO}_2 + \text{n-decane}$  system increased with increasing temperature<sup>37,40,41,50</sup>. This can be explained by the fact that the local adsorption of gas molecules at the interface is more pronounced for carbon dioxide when compared to that of methane, especially at low temperatures. It is to be noted that, the investigation of ternary mixtures containing methane, carbon dioxide, and higher alkanes has been rare<sup>57</sup>.

Molecular simulations provide valuable insights into the bulk and interfacial properties of various systems<sup>14–17,58–63</sup>. In this work, we perform molecular dynamics (MD) simulations to understand the properties of  $\text{CH}_4 + \text{n-decane}$ ,  $\text{CO}_2 + \text{n-decane}$ , and  $\text{CH}_4 + \text{CO}_2 + \text{n-decane}$  systems over a broad range of temperature (313–442 K) and pressure (up to about 300 bar) relevant to geological processes. Given the general lack of experimental results for these systems, especially the ternary case, theoretical modeling is employed to complement the simulation data.

## Methods

**Simulation details.** The MD simulation was carried out using the GROMACS code<sup>64</sup>. The simulation model and method used here are similar to the ones reported in our previous work<sup>14,63</sup>. The transferable potentials for phase equilibria force field<sup>65</sup> was used to model n-decane, methane, and  $\text{CO}_2$ . The simulations were initiated by placing 400 decane molecules and up to 2048  $\text{CH}_4/\text{CO}_2$  molecules in each simulation box. In directions parallel to the interface, each cell was about  $50 \times 50 \text{ \AA}$ , and periodic boundary conditions were used in all directions (Fig. 1). These values were chosen to ensure reasonable bulk phases with enough molecules and also to reduce the truncation and system size effects in the calculations of the bulk and interfacial properties<sup>39,46,52–56</sup>. These systems are energy-minimized using the steepest descent algorithm and subjected to equilibration MD runs of 10 ns in the  $NPT$  ensemble. During the  $NPT$  runs, the volume changes are obtained by adjusting only the cell size in the  $z$  direction ( $L_z$ ) normal to the interface. After that we carried out production runs of 6 ns duration in the  $NVE$  ensemble. The leap-frog algorithm<sup>66</sup> with a time step of 1 fs was used to integrate the equations of motion. The linear constraint solver algorithm<sup>67</sup> was implemented to constrain the bond lengths and angles. Virtual sites were used to maintain the rigid structure of  $\text{CO}_2$ <sup>68</sup>. The particle mesh Ewald method was used to calculate the long-range electrostatic interactions. The Nosé-Hoover thermostat and Parrinello-Rahman barostat, with a relaxation time of 2.0 ps for both, were used to regulate the temperature and pressure, respectively. Each MD run was repeated three times and the average value was taken.

The IFT was calculated as follows<sup>52,63</sup>:

$$\gamma = \frac{1}{2}L_z \left[ P_{zz} - \frac{1}{2}(P_{xx} + P_{yy}) \right], \quad (1)$$

where  $P_{xx}$ ,  $P_{yy}$ , and  $P_{zz}$  are the three diagonal components of the pressure tensor. Typically, for the estimation of various atomic density profiles, a bin width of 1 Å is used.

**Theoretical details.** The volume translated predictive Peng-Robinson 1978 (VT-PPR78)<sup>40,44,69</sup> equation of state (EoS) with the usual van der Waals one-fluid mixing rules and a linear mixing rule for the volume correction is used to estimate bulk properties. The VT-PPR78 model calculates the binary interaction parameter  $k_{ij}$  for each temperature using a group contribution method. Additionally, the interfacial properties were calculated by coupling the VT-PPR78 EoS with the density gradient theory (DGT). In brief, the Helmholtz free energy of the planar interface is given by<sup>70,71</sup>

$$F = A \int_{-\infty}^{+\infty} \left[ f_0(n) + \frac{1}{2} \sum_i \sum_j c_{ij} \frac{dn_i}{dz} \frac{dn_j}{dz} \right] dz, \quad (2)$$

where  $A$  is the area of the planar interface,  $f_0$  represents the Helmholtz free energy density of the homogeneous fluid at the local density  $n$ ,  $dn_i/dz$  is the local gradient in density of a given component  $i$ , and  $c_{ij}$  is the cross influence parameter defined as follows:

$$c_{ij} = (1 - \beta_{ij}) \sqrt{c_{ii} c_{jj}}, \quad (3)$$

where  $c_{ii}$  and  $c_{jj}$  denote the pure component influence parameters, and  $\beta_{ij}$  represents the binary interaction coefficient. In this study, the pure component influence parameter is computed based on the correlation developed by Miquieu *et al.*<sup>44</sup>. The minimization of the Helmholtz free energy leads to the following Euler-Lagrange equations:

$$\sum_j c_{ij} \frac{d^2 n_j}{dz^2} = \mu_i^0(n_1(z), \dots, n_{N_c}(z)) - \mu_i \text{ for } i, j = 1, \dots, N_c, \quad (4)$$

where  $\mu_i^0 \equiv \left( \frac{\partial f_0}{\partial n_i} \right)_{T, V, n_j}$ ,  $\mu_i$  denotes the chemical potential of component  $i$  in the equilibrium bulk phase and  $N_c$  represents the total number of components. To obtain the density profiles across the interface, the above set of equations must be solved together with the following boundary conditions:

$$\begin{aligned} n_i(-\infty) &= n_i^I \\ n_i(+\infty) &= n_i^{II} \end{aligned} \quad (5)$$

where  $n_i^I$  and  $n_i^{II}$  are the equilibrium densities of component  $i$  in the coexisting bulk phases. As stated above, the bulk properties are calculated using the VT-PPR78 EoS. Using the geometric mixing rule ( $\beta_{ij}=0$ ) reduces the system of  $N_c$  differential equations (Eq. (4)) to the system of  $(N_c - 1)$  algebraic equations:

$$\sqrt{c_i} (\mu_{\text{ref}}^0(n(z)) - \mu_{\text{ref}}) = \sqrt{c_{\text{ref}}} (\mu_i^0(n(z)) - \mu_i); \quad i = 1, \dots, N_c, \text{ and } i \neq \text{ref}. \quad (6)$$

These equations could compute the densities of all except one component and the density of the latter is monotonic function of  $z$  over the whole interface<sup>40,44</sup> and used as a reference variable. Once the density profiles are known, the IFT can be calculated using the following equation:

$$\gamma = \int_{n_{\text{ref}}^I}^{n_{\text{ref}}^{II}} \sqrt{2\Delta\Omega(n) \sum_i \sum_j c_{ij} \frac{dn_i}{dn_{\text{ref}}} \frac{dn_j}{dn_{\text{ref}}}} dn_{\text{ref}}, \quad (7)$$

where

$$\Delta\Omega = f_0(n) - \sum_i n_i \mu_i + P. \quad (8)$$

Note that,  $\Delta\Omega(n) = \Omega(n) - \Omega_B$  is the difference between the grand thermodynamic potential  $\Omega \equiv f_0(n) - \sum_i n_i \mu_i$  at the local density and its value in the bulk phase  $\Omega_B = -P$ . Furthermore, the  $z$ -coordinate for the density profile can be computed using the following equation:

$$z = z_0 + \int_{n_{\text{ref}}^0}^{n_{\text{ref}}(z)} \sqrt{\frac{\sum_i \sum_j c_{ij} \frac{dn_i}{dn_{\text{ref}}} \frac{dn_j}{dn_{\text{ref}}}}{2\Delta\Omega(n)}} dn_{\text{ref}}, \quad (9)$$

where  $z_0$  and  $n_{\text{ref}}^0$  represent the coordinate and the density, respectively, arbitrarily chosen as origins.

## Results

**Atomic density profiles.** Both MD simulations and DFT calculations were used to predict the atomic density profiles that are not always easily accessible to experiments. For instance, Fig. 2 displays the density profiles of various species as obtained from the MD simulations (solid lines) and the corresponding theoretical data (dashed lines) for CH<sub>4</sub> + n-decane, CO<sub>2</sub> + n-decane, and CH<sub>4</sub> + CO<sub>2</sub> + n-decane (equimolar CH<sub>4</sub>/CO<sub>2</sub> mixture) systems at 343 K. We see that the simulation results are in good qualitative agreement with the theoretical data. Note that among the different species, the maximum difference (differ by a factor of up to ~2) between the simulated and calculated densities is obtained for CO<sub>2</sub>, especially at high pressures. In all cases, the density profiles show local enrichment of gas molecules at the interface, but no such behavior is seen for n-decane in agreement with the previous studies<sup>38-41,43-53</sup>. That is, a positive surface activity is seen for both methane and carbon dioxide ( $dn_i/dz = 0$ ;  $d^2n_i/dz^2 < 0$  in the interfacial region). Whereas the density profile of decane across the interface varies monotonically and does not show surface activity. Also, the higher methane and/or carbon dioxide contents result in a broadening of the interface. As seen from the adsorption peaks in Fig. 2, the local accumulations of methane and carbon dioxide, in general, increase with pressure. However, at high pressures, the local enrichment of gas molecules decreases with pressure. It is known that the local enrichment of the interface in methane and carbon dioxide typically decreases with temperature<sup>38-40,43-49,52,53</sup>. The density of CO<sub>2</sub> is usually higher in the liquid phase

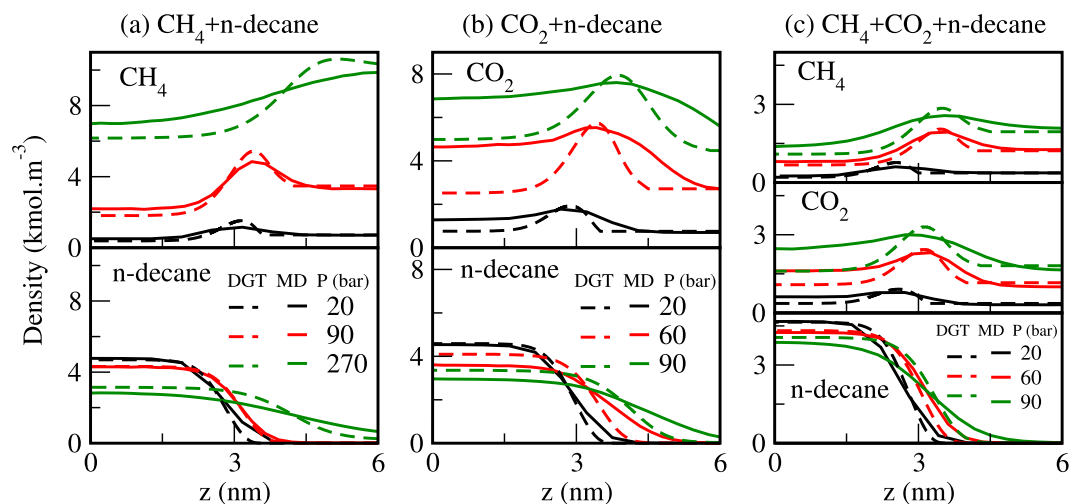


**Figure 2.** Atomic density profiles for (a)  $\text{CH}_4$  + n-decane, (b)  $\text{CO}_2$  + n-decane, and (c)  $\text{CH}_4$  +  $\text{CO}_2$  + n-decane systems at 343 K. The solid lines represent the results from the MD simulations and the estimates obtained using the DGT with VT-PPR78 EoS are shown as dashed lines.

(decane-rich) when compared to that in the  $\text{CO}_2$ -rich phase, whereas an opposite trend is found for methane. Our results also show the preferential dissolution in the decane-rich phase and adsorption at the interface for carbon dioxide from the  $\text{CH}_4/\text{CO}_2$  mixture.

**Bulk properties.** Figure 3 shows the bulk densities as obtained from the MD simulations (open symbols) and the corresponding theoretical data (solid lines) for  $\text{CH}_4$  + n-decane,  $\text{CO}_2$  + n-decane, and  $\text{CH}_4$  +  $\text{CO}_2$  + n-decane (equimolar  $\text{CH}_4/\text{CO}_2$  mixture) systems under geological conditions. These results are also compared with the corresponding experimental data<sup>40</sup> (closed symbols). Other experimental data<sup>30,32,33,35,39</sup> are similar to the ones plotted here and not shown for clarity. Note that in the absence of any experimental data, the simulation results of the  $\text{CH}_4$  +  $\text{CO}_2$  + n-decane system are only compared with the theoretical predictions. We see that both our theoretical and simulation results are in good agreement with the experimental data. For example, the overall absolute average deviation between theoretical and experimental density values is less than about 2% in the decane-rich phase, while it is less than about 3% in the  $\text{CH}_4$ -rich or  $\text{CO}_2$ -rich phase. In all cases, these total densities generally decrease with temperature in both phases. Also, these densities generally decrease with pressure in the decane-rich phase and increase with pressure in the  $\text{CH}_4$ -rich and/or  $\text{CO}_2$ -rich phases. However, for example, in the  $\text{CO}_2$  + n-decane system, the density of the decane-rich phase increases with pressure, especially at low temperatures and pressures. These different scenarios may take place depending on the gas solubility and swelling in the decane-rich phase.

The knowledge of the species mole fractions and swelling effects plays an important role in the use of carbon dioxide for the recovery of hydrocarbon fluids from underground reservoirs<sup>30,32,40,53,56</sup>. Figure 4 shows the bulk mole fractions of methane and carbon dioxide in the decane-rich phase as obtained from the MD simulations (open symbols) and the corresponding theoretical data (solid lines) for all studied systems. These results are also compared with the experimental data<sup>30,32</sup> (closed symbols). Both our theoretical and simulation results are again consistent with the experimental data. In general, various mole fractions for all studied systems increase with increasing pressure and decreasing temperature. Notably, the mole fraction of methane in these systems is not significantly affected by temperature. Overall, the amount of n-decane in the  $\text{CH}_4$ -rich and/or  $\text{CO}_2$ -rich phases was estimated to be relatively small (see, e.g., Fig. 2).

Furthermore, Fig. 5 shows the swelling factor for the decane-rich phase as obtained from the MD simulations (open symbols) and the corresponding theoretical data (solid lines) for all studied systems. The swelling factor is defined as ratio of the volume of the saturated decane-rich system to the volume of the decane alone<sup>53,56</sup>. Though not shown, both theoretical and simulation results for densities of the pure n-decane system at the studied conditions are in good quantitative agreement with the NIST data<sup>72</sup>. In general, the swelling factor for all the studied systems increases with increasing pressure and decreasing temperature, which is consistent with the above solubility data. Also, similar to the solubility vs temperature behavior, the swelling of the  $\text{CH}_4$  + n-decane system is not significantly affected by temperature. It is known that the interaction between  $\text{CO}_2$  and alkane molecules plays a key role in the solubility and swelling properties of the alkane- $\text{CO}_2$  system<sup>53,56</sup>. For example, Fig. 6 shows the radial distribution functions between decane (carbon site) and  $\text{CH}_4/\text{CO}_2$  in the bulk liquid phase of the  $\text{CH}_4$  +  $\text{CO}_2$  + n-decane system at 343 K and 60 bar. These results were obtained using an NPT MD simulation of the corresponding bulk liquid phase alone. From this figure, it can be seen that  $\text{CO}_2$  molecules are positioned relatively close to decane. Furthermore, for this system, we find that the interaction energies of decane- $\text{CO}_2$  and decane- $\text{CH}_4$  are about  $-2428.5$  and  $-930.9$  kJ/mol, respectively. All these results indicate the preferential interaction of decane with  $\text{CO}_2$  relative to  $\text{CH}_4$ .

The conformation of the n-decane molecule may be characterized by its radius of gyration  $R_g$ <sup>54,55,61</sup>. The  $R_g$  is defined as the root-mean-square distance of all atoms from their common center of mass. The  $R_g$  was calculated

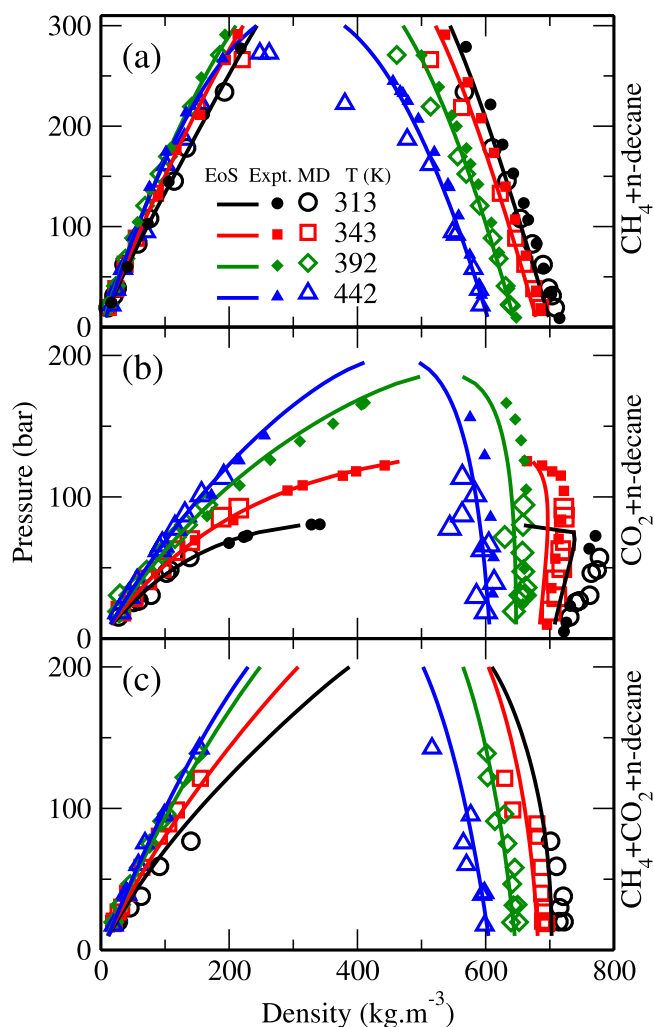


**Figure 3.** Saturated densities for (a)  $\text{CH}_4 + \text{n-decane}$ , (b)  $\text{CO}_2 + \text{n-decane}$ , and (c)  $\text{CH}_4 + \text{CO}_2 + \text{n-decane}$  systems. The open symbols represent the results from the MD simulations and the estimates obtained using the VT-PPR78 EoS are shown as lines. The experimental results of Pereira *et al.*<sup>40</sup> are shown as solid symbols. The error bars are smaller than the symbol size.

from the MD simulations in order to check the compactness of the conformations. Our calculations find that the  $R_g$  values decrease with increasing temperature and are in the range of 0.32–0.34 nm for all systems. This is because as the temperature increases, the effective monomer-monomer attraction becomes increasingly important, causing the chains to shrink<sup>54</sup>. The values of  $R_g$  are in good agreement with the previous reported results<sup>54,55</sup>. We also find that the  $R_g$  is much less sensitive to changes in pressure and to the presence of methane and  $\text{CO}_2$ .

**Interfacial properties.** Figure 7 shows the IFTs as obtained from the MD simulations (open symbols) and the corresponding theoretical data (solid lines) for  $\text{CH}_4 + \text{n-decane}$ ,  $\text{CO}_2 + \text{n-decane}$ , and  $\text{CH}_4 + \text{CO}_2 + \text{n-decane}$  (equimolar  $\text{CH}_4/\text{CO}_2$  mixture) systems under geological conditions. These results are also compared with the corresponding experimental data<sup>40</sup> (closed symbols). Other experimental data<sup>31,33–35,37,39,41</sup> are similar to the ones plotted here and not shown for clarity. Note that in the absence of any experimental data, the simulation results of the  $\text{CH}_4 + \text{CO}_2 + \text{n-decane}$  system are only compared with the theoretical predictions. In the temperature range (313–442 K) considered here, the surface tension of pure n-decane decreases from about 22 to 11 mN/m<sup>72</sup>. It can be seen that both our theoretical and simulation results are in good agreement with the experimental estimates. For example, the overall absolute average deviation between theoretical and experimental IFT values is less than about 9%. These results show that, at a given temperature and pressure, the presence of  $\text{CH}_4$  increases the IFT of the  $\text{CO}_2 + \text{n-decane}$  system. The IFT of  $\text{CH}_4 + \text{n-decane}$ ,  $\text{CO}_2 + \text{n-decane}$ , and  $\text{CH}_4 + \text{CO}_2 + \text{n-decane}$  systems decreases with pressure. In general, a similar trend is observed for the temperature dependence of the IFT. However at high pressures, for example, the IFT of the  $\text{CO}_2 + \text{n-decane}$  system increases with increasing temperature. This can be described<sup>40</sup> by the fact that the local enrichment of gas molecules at the interface (see, e.g., Fig. 2) is more pronounced for carbon dioxide when compared to that of methane, especially at low temperatures. The correlation between the IFT and the local enrichment of the interface in methane and carbon dioxide will be discussed in detail below. Notably, theoretical calculations based on other equations of state<sup>38–41,43–51</sup>, such as the statistical associating fluid theory, can also give accurate estimates of the bulk and interfacial properties of these

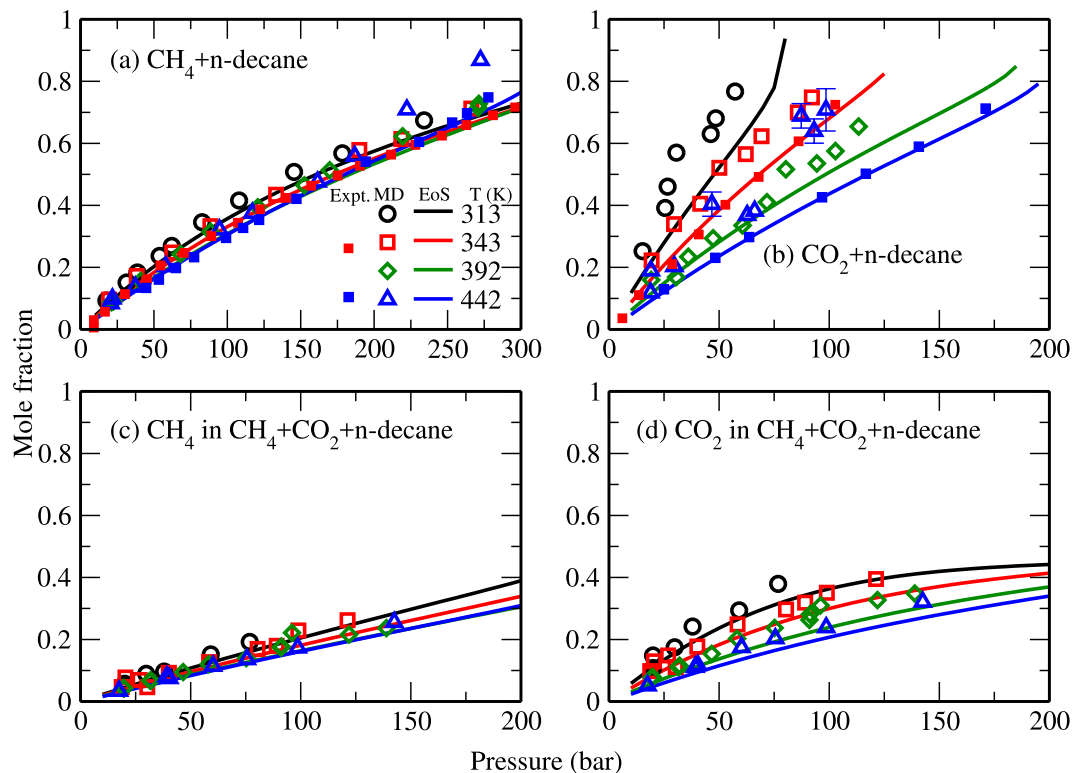


**Figure 4.** Mole fractions of CH<sub>4</sub> and CO<sub>2</sub> in the decane-rich phase: (a) CH<sub>4</sub> in CH<sub>4</sub> + n-decane, (b) CO<sub>2</sub> in CO<sub>2</sub> + n-decane, (c) CH<sub>4</sub> in CH<sub>4</sub> + CO<sub>2</sub> + n-decane, and (d) CO<sub>2</sub> in CH<sub>4</sub> + CO<sub>2</sub> + n-decane systems. The symbols are the same as in Fig. 3. Note that here the experimental data were taken from Reamer *et al.*<sup>30,32</sup>.

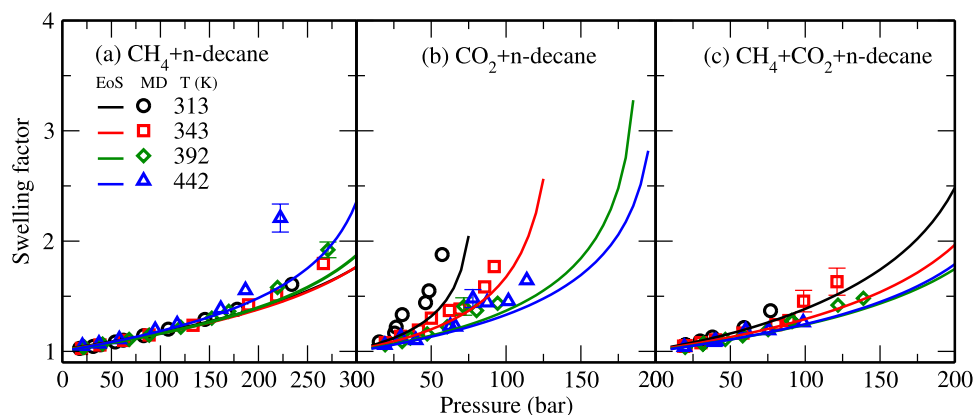


**Figure 5.** Swelling factor of (a) CH<sub>4</sub> + n-decane, (b) CO<sub>2</sub> + n-decane, and (c) CH<sub>4</sub> + CO<sub>2</sub> + n-decane systems. The symbols are the same as in Fig. 3.

binary systems. One of the main properties governing the design and operation of CCS and EOR processes is the miscibility of the injected CO<sub>2</sub> with oil<sup>24,36</sup>. The minimum miscibility pressure is taken as a pressure at which the IFT becomes zero<sup>36</sup>. Due to the fact that the IFT of the CO<sub>2</sub> + n-decane system decreases steeply with increasing pressure, pure CO<sub>2</sub> is completely miscible with decane from relatively low pressures. In the presence of methane, the CO<sub>2</sub> + decane system seems to indicate a smaller miscibility region with respect to pressure.

## Discussion

The results obtained in this study allow one to quantify the local enrichment of the interface in methane and carbon dioxide. In this context, it is important to notice that the IFT is related to the surface excess  $\Gamma_i$  as given by the Gibbs adsorption equation<sup>40,63</sup>:



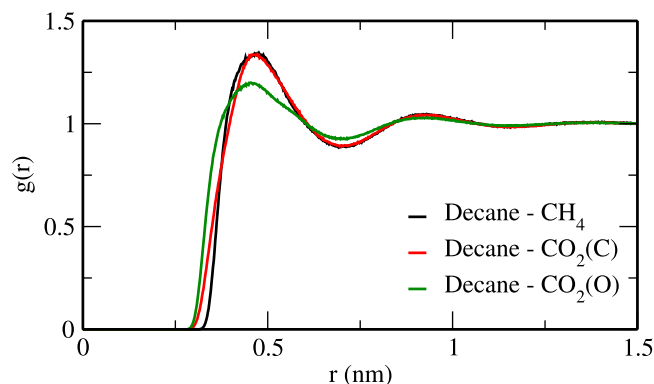


**Figure 6.** Radial distribution functions between decane and CH<sub>4</sub>/CO<sub>2</sub> in the bulk liquid phase of the CH<sub>4</sub> + CO<sub>2</sub> + n-decane system at 343 K and 60 bar.

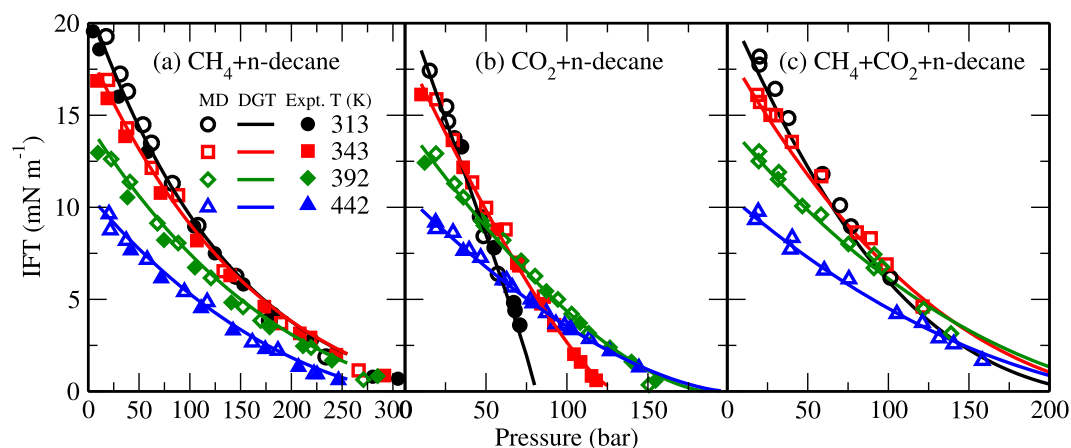


**Figure 7.** IFTs of (a) CH<sub>4</sub> + n-decane, (b) CO<sub>2</sub> + n-decane, and (c) CH<sub>4</sub> + CO<sub>2</sub> + n-decane systems. The open symbols represent the results from the MD simulations and the estimates obtained using the DGT with VT-PPR78 EoS are shown as lines. The experimental results of Pereira *et al.*<sup>40</sup> are shown as solid symbols.

$$-d\gamma = \sum_i \Gamma_i d\mu_i. \quad (10)$$

The surface excess of a component  $i$  with respect to decane is given by

$$\Gamma_{i,\text{decane}} = -\alpha_i \int_{-\infty}^{+\infty} \Delta C(z) dz, \quad (11)$$

with

$$\Delta C(z) = \frac{n_{\text{decane}}(z) - n_{\text{decane}}^{\text{II}}}{\alpha_{\text{decane}}} - \frac{n_i(z) - n_i^{\text{II}}}{\alpha_i}, \quad (12)$$

where

$$\alpha_i = \frac{n_i^{\text{II}} - n_i^{\text{I}}}{n_i^{\text{II}} - n_i^{\text{I}} + n_{\text{decane}}^{\text{II}} - n_{\text{decane}}^{\text{I}}}, \quad (13)$$

and

$$\alpha_{\text{decane}} = \frac{n_{\text{decane}}^{\text{II}} - n_{\text{decane}}^{\text{I}}}{n_i^{\text{II}} - n_i^{\text{I}} + n_{\text{decane}}^{\text{II}} - n_{\text{decane}}^{\text{I}}}. \quad (14)$$

Here,  $I$  represents the CH<sub>4</sub>-rich and/or CO<sub>2</sub>-rich phases, and  $II$  the decane-rich phase. Figure 8 shows the surface excesses of CH<sub>4</sub> and CO<sub>2</sub> as obtained from the MD simulations (open symbols) and the corresponding theoretical data (solid lines) for all studied systems. These results are also compared with the experimental

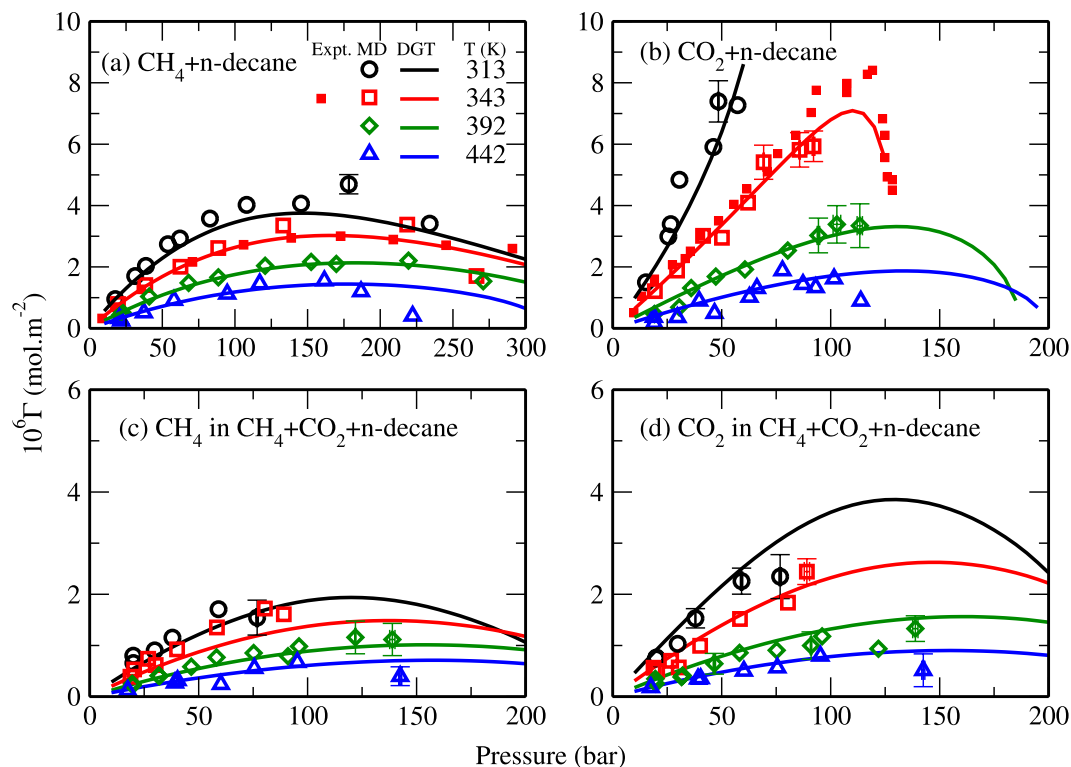


**Figure 8.** Surface excess of (a)  $\text{CH}_4$  in  $\text{CH}_4 + \text{n-decane}$ , (b)  $\text{CO}_2$  in  $\text{CO}_2 + \text{n-decane}$ , (c)  $\text{CH}_4$  in  $\text{CH}_4 + \text{CO}_2 + \text{n-decane}$ , and (d)  $\text{CO}_2$  in  $\text{CH}_4 + \text{CO}_2 + \text{n-decane}$  systems. The symbols are the same as in Fig. 7.

data<sup>35,40</sup> (closed symbols). In all cases, we see a nonmonotonic variation of the surface excess with pressure. The relatively higher surface excess of the  $\text{CO}_2 + \text{n-decane}$  system results in a steeper decrease in its IFT as a function of pressure (see also Eq. (10) and Fig. 7). Overall, the surface excesses decrease with increasing temperature and the results of the ternary system fall between those of the binary systems.

To conclude, we have studied using MD simulations the bulk and interfacial properties of  $\text{CH}_4 + \text{n-decane}$ ,  $\text{CO}_2 + \text{n-decane}$ , and  $\text{CH}_4 + \text{CO}_2 + \text{n-decane}$  systems under geological conditions. Theoretical modeling using the VT-PPR78 EoS combined with DGT was employed to complement the simulation data. The simulation results of the atomic density profiles and the IFT values are in good agreement with both the theoretical and experimental data. The results of our study show that, in general, the local accumulations of methane and carbon dioxide increase with increasing pressure and decreasing temperature. At high pressures, however, the local enrichment of gas molecules decreases with pressure. An important result is the preferential dissolution in the decane-rich phase and adsorption at the interface for carbon dioxide from the  $\text{CH}_4/\text{CO}_2$  mixture. The gas solubility and swelling in the decane-rich phase can play a key role in determining the behavior of the bulk densities as a function of temperature and pressure. Typically, both the gas solubility and the swelling factor for all the studied systems increase with increasing pressure and decreasing temperature. Notably, the mole fraction of methane and the swelling of the  $\text{CH}_4 + \text{n-decane}$  system are not significantly affected by temperature. Furthermore, we find that the presence of  $\text{CH}_4$  increases the IFT of the  $\text{CO}_2 + \text{n-decane}$  system. The IFT of the investigated systems decreases with pressure. In general, a similar trend was observed for the temperature dependence of the IFT. However, at high pressures the IFT of, e.g., the  $\text{CO}_2 + \text{n-decane}$  system increases with temperature. There is a nonmonotonic variation of the surface excess with pressure and it decreases with temperature. The surface excess is more pronounced for carbon dioxide when compared to that of methane in the studied systems. Because of this fact, the IFT decreases steeply with increasing pressure for systems containing  $\text{CO}_2$ .

Received: 4 October 2019; Accepted: 5 December 2019;

Published online: 24 December 2019

## References

1. Birol, F.  $\text{CO}_2$  Emissions from fuel combustion highlights (2016).
2. Houghton, E. *Climate change 1995: The science of climate change: contribution of working group I to the second assessment report of the Intergovernmental Panel on Climate Change*, vol. 2 (Cambridge University Press, 1996).
3. Cox, P. M., Betts, R. A., Jones, C. D., Spall, S. A. & Totterdell, I. J. Acceleration of global warming due to carbon-cycle feedbacks in a coupled climate model. *Nature* **408**, 184 (2000).
4. Stocker, T. F. *et al.* *Climate change 2013: The physical science basis* (2013).
5. Moore, J. C., Gladstone, R., Zwinger, T. & Wolovick, M. Geoengineer polar glaciers to slow sea-level rise (2018).
6. Rhodes, C. J. The 2015 paris climate change conference: Cop21. *Science progress* **99**, 97–104 (2016).
7. Sumida, K. *et al.* Carbon dioxide capture in metal-organic frameworks. *Chemical reviews* **112**, 724–781 (2011).



8. Rangnekar, N., Mittal, N., Elyassi, B., Caro, J. & Tsapatsis, M. Zeolite membranes—a review and comparison with mofs. *Chemical Society Reviews* **44**, 7128–7154 (2015).
9. D'Alessandro, D. M., Smit, B. & Long, J. R. Carbon dioxide capture: prospects for new materials. *Angewandte Chemie International Edition* **49**, 6058–6082 (2010).
10. Yang, H. *et al.* Progress in carbon dioxide separation and capture: A review. *Journal of environmental sciences* **20**, 14–27 (2008).
11. Phan, A. *et al.* Synthesis, structure, and carbon dioxide capture properties of zeolitic imidazolate frameworks (2009).
12. Yampolskii, Y. Polymeric gas separation membranes. *Macromolecules* **45**, 3298–3311 (2012).
13. Kupgan, G., Abbott, L. J., Hart, K. E. & Colina, C. M. Modeling amorphous microporous polymers for CO<sub>2</sub> capture and separations. *Chemical reviews* **118**, 5488–5538 (2018).
14. Yang, Y., Narayanan Nair, A. K. & Sun, S. Adsorption and diffusion of methane and carbon dioxide in amorphous regions of cross-linked polyethylene: a molecular simulation study. *Industrial & Engineering Chemistry Research* (2019).
15. Kadoura, A., Nair, A. K. N. & Sun, S. Adsorption of carbon dioxide, methane, and their mixture by montmorillonite in the presence of water. *Microporous and Mesoporous Materials* **225**, 331–341 (2016).
16. Kadoura, A., Narayanan Nair, A. K. & Sun, S. Molecular dynamics simulations of carbon dioxide, methane, and their mixture in montmorillonite clay hydrates. *The Journal of Physical Chemistry C* **120**, 12517–12529 (2016).
17. Kadoura, A., Narayanan Nair, A. K. & Sun, S. Molecular simulation study of montmorillonite in contact with variably wet supercritical carbon dioxide. *The Journal of Physical Chemistry C* **121**, 6199–6208 (2017).
18. Romanov, V. *Greenhouse Gases and Clay Minerals: Enlightening Down-to-Earth Road Map to Basic Science of Clay-Greenhouse Gas Interfaces* (Springer, 2017).
19. Orr, J. F. & Taber, J. Use of carbon dioxide in enhanced oil recovery. *Science* **224**, 563–569 (1984).
20. Langston, M. *et al.* Definitive CO<sub>2</sub> flooding response in the sacroc unit. In *SPE Enhanced Oil Recovery Symposium* (Society of Petroleum Engineers, 1988).
21. Blunt, M., Fayers, F. J. & Orr, F. M. Jr. Carbon dioxide in enhanced oil recovery. *Energy Conversion and Management* **34**, 1197–1204 (1993).
22. Gozalspour, F., Ren, S. R. & Tohidi, B. CO<sub>2</sub> EOR and storage in oil reservoir. *Oil & gas science and technology* **60**, 537–546 (2005).
23. DiPietro, P., Balash, P. & Wallace, M. A note on sources of CO<sub>2</sub> supply for enhanced-oil-recovery operations. *SPE Economics & Management* **12**, 1652–1654 (2012).
24. Enick, R. M. & Olsen, D. K. Mobility and conformance control for carbon dioxide enhanced oil recovery (CO<sub>2</sub>-EOR) via thickeners, foams, and gels—a detailed literature review of 40 years of research. *Contract DE-FE0004003. Activity* **4003** (2012).
25. Verma, M. K. *Fundamentals of carbon dioxide-enhanced oil recovery (CO<sub>2</sub>-EOR): A supporting document of the assessment methodology for hydrocarbon recovery using CO<sub>2</sub>-EOR associated with carbon sequestration* (US Department of the Interior, US Geological Survey Washington, DC, 2015).
26. EIA, U. Annual energy outlook 2015: with projections to 2040 (2017).
27. Olajire, A. A. CO<sub>2</sub> capture and separation technologies for end-of-pipe applications—a review. *Energy* **35**, 2610–2628 (2010).
28. Li, H., Jakobsen, J. P., Wilhelmsen, Ø. & Yan, J. PVTX properties of CO<sub>2</sub> mixtures relevant for CO<sub>2</sub> capture, transport and storage: Review of available experimental data and theoretical models. *Applied Energy* **88**, 3567–3579 (2011).
29. Blanco, S. T., Rivas, C., Fernandez, J., Artal, M. & Velasco, I. Influence of methane in CO<sub>2</sub> transport and storage for CCS technology. *Environmental science & technology* **46**, 13016–13023 (2012).
30. Reamer, H., Olds, R., Sage, B. & Lacey, W. Phase equilibria in hydrocarbon systems. *Industrial & Engineering Chemistry* **34**, 1526–1531 (1942).
31. Stegemeier, G. L. *et al.* Interfacial tension of the methane-normal decane system. *Society of Petroleum Engineers Journal* **2**, 257–260 (1962).
32. Reamer, H. & Sage, B. Phase equilibria in hydrocarbon systems. volumetric and phase behavior of the n-decane-CO<sub>2</sub> system. *Journal of Chemical and Engineering Data* **8**, 508–513 (1963).
33. Nagarajan, N. & Robinson, R. L. Jr. Equilibrium phase compositions, phase densities, and interfacial tensions for carbon dioxide + hydrocarbon systems. 2. carbon dioxide + n-decane. *Journal of Chemical and Engineering Data* **31**, 168–171 (1986).
34. Amin, R. & Smith, T. N. Interfacial tension and spreading coefficient under reservoir conditions. *Fluid phase equilibria* **142**, 231–241 (1998).
35. Shaver, R., Robinson, R. Jr. & Gasem, K. An automated apparatus for equilibrium phase compositions, densities, and interfacial tensions: data for carbon dioxide + decane. *Fluid phase equilibria* **179**, 43–66 (2001).
36. Ayrala, S. C., Xu, W. & Rao, D. N. Interfacial behaviour of complex hydrocarbon fluids at elevated pressures and temperatures. *The Canadian Journal of Chemical Engineering* **84**, 22–32 (2006).
37. Georgiadis, A. *et al.* Interfacial tension measurements and modelling of (carbon dioxide + n-alkane) and (carbon dioxide + water) binary mixtures at elevated pressures and temperatures. *The Journal of Supercritical Fluids* **55**, 743–754 (2010).
38. Cumicheo, C., Cartes, M., Segura, H., Müller, E. A. & Mejia, A. High-pressure densities and interfacial tensions of binary systems containing carbon dioxide + n-alkanes: (n-dodecane, n-tridecane, n-tetradecane). *Fluid Phase Equilibria* **380**, 82–92 (2014).
39. Mejia, A., Cartes, M., Segura, H. & Müller, E. A. Use of equations of state and coarse grained simulations to complement experiments: describing the interfacial properties of carbon dioxide + decane and carbon dioxide + eicosane mixtures. *Journal of Chemical & Engineering Data* **59**, 2928–2941 (2014).
40. Pereira, L. M., Chapoy, A., Burgass, R. & Tohidi, B. Measurement and modeling of high pressure density and interfacial tension of (gas + n-alkane) binary mixtures. *The Journal of Chemical Thermodynamics* **97**, 55–69 (2016).
41. Li, N. *et al.* Interfacial tension measurement and calculation of (carbon dioxide + n-alkane) binary mixtures. *Journal of Chemical & Engineering Data* **62**, 2861–2871 (2017).
42. Bagalkot, N. & Hamouda, A. A. Experimental and numerical method for estimating diffusion coefficient of the carbon dioxide into light components. *Industrial & Engineering Chemistry Research* **56**, 2359–2374 (2017).
43. Sahimi, M. & Taylor, B. N. Surface tension of binary liquid–vapor mixtures: A comparison of mean-field and scaling theories. *The Journal of chemical physics* **95**, 6749–6761 (1991).
44. Miqueu, C., Mendiboure, B., Graciaa, A. & Lachaise, J. Modelling of the surface tension of pure components with the gradient theory of fluid interfaces: a simple and accurate expression for the influence parameters. *Fluid phase equilibria* **207**, 225–246 (2003).
45. Li, Z. & Firoozabadi, A. Interfacial tension of nonassociating pure substances and binary mixtures by density functional theory combined with peng–robinson equation of state. *The Journal of chemical physics* **130**, 154108 (2009).
46. Müller, E. A. & Mejia, A. Interfacial properties of selected binary mixtures containing n-alkanes. *Fluid Phase Equilibria* **282**, 68–81 (2009).
47. Amézquita, O. N., Enders, S., Jaeger, P. & Eggers, R. Interfacial properties of mixtures containing supercritical gases. *The Journal of supercritical fluids* **55**, 724–734 (2010).
48. Llovel, F., Mac Dowell, N., Blas, F. J., Galindo, A. & Jackson, G. Application of the soft-vr density functional theory to the prediction of the interfacial properties of mixtures of relevance to reservoir engineering. *Fluid Phase Equilibria* **336**, 137–150 (2012).
49. Prieto, M. G., Sanchez, F. A. & Pereda, S. Multiphase equilibria modeling with gca-eos. part I: Carbon dioxide with the homologous series of alkanes up to 36 carbons. *Industrial & Engineering Chemistry Research* **54**, 12415–12427 (2015).
50. Garrido, J. M. & Polishuk, I. Toward development of a universal cp–pc–saftbased modeling framework for predicting thermophysical properties at reservoir conditions: inclusion of surface tensions. *Industrial & Engineering Chemistry Research* **57**, 8819–8831 (2018).

51. Camacho Vergara, E. L., Kontogeorgis, G. M. & Liang, X. Gas adsorption and interfacial tension with classical density functional theory. *Industrial & Engineering Chemistry Research* **58**, 5650–5664 (2019).
52. Neyt, J.-C., Wender, A., Lachet, V. & Malfreyt, P. Modeling the pressure dependence of acid gas + n-alkane interfacial tensions using atomistic monte carlo simulations. *The Journal of Physical Chemistry C* **116**, 10563–10572 (2012).
53. Liu, B. *et al.* Molecular dynamics simulation on volume swelling of Co<sub>2</sub>-alkane system. *Fuel* **143**, 194–201 (2015).
54. Mondello, M. & Grest, G. S. Molecular dynamics of linear and branched alkanes. *The Journal of chemical physics* **103**, 7156–7165 (1995).
55. Moultois, O. A., Tsimpanogiannis, I. N., Panagiotopoulos, A. Z., Trusler, J. M. & Economou, I. G. Atomistic molecular dynamics simulations of carbon dioxide diffusivity in n-hexane, n-decane, n-hexadecane, cyclohexane, and squalane. *The Journal of Physical Chemistry B* **120**, 12890–12900 (2016).
56. Li, C., Pu, H. & Zhao, J. X. Molecular simulation study on the volume swelling and the viscosity reduction of n-alkane/co<sub>2</sub> systems. *Industrial & Engineering Chemistry Research* (2019).
57. Jaeger, P. T. & Eggers, R. Interfacial properties at elevated pressures in reservoir systems containing compressed or supercritical carbon dioxide. *The Journal of Supercritical Fluids* **66**, 80–85 (2012).
58. Kumar, N. A. & Seidel, C. Polyelectrolyte brushes with added salt. *Macro-molecules* **38**, 9341–9350 (2005).
59. Kumar, N. A. & Ganesan, V. Communication: Self-assembly of semiexible-exible block copolymers (2012).
60. Stukalin, E. B., Cai, L.-H., Kumar, N. A., Leibler, L. & Rubinstein, M. Selfhealing of unentangled polymer networks with reversible bonds. *Macromolecules* **46**, 7525–7541 (2013).
61. Narayanan Nair, A. K., Martinez Jimenez, A. & Sun, S. Complexation behavior of polyelectrolytes and polyampholytes. *The Journal of Physical Chemistry B* **121**, 7987–7998 (2017).
62. Li, Y., Narayanan Nair, A. K., Kadoura, A., Yang, Y. & Sun, S. Molecular simulation study of montmorillonite in contact with water. *Industrial & Engineering Chemistry Research* **58**, 1396–1403 (2019).
63. Yang, Y., Che Ruslan, M. F. A., Narayanan Nair, A. K. & Sun, S. Effect of ion valency on the properties of the carbon dioxide-methane-brine system. *The Journal of Physical Chemistry B* **123**, 2719–2727 (2019).
64. Abraham, M. J. *et al.* Gromacs: High performance molecular simulations through multi-level parallelism from laptops to supercomputers. *SoftwareX* **1**, 19–25 (2015).
65. Martin, M. G. & Siepmann, J. I. Transferable potentials for phase equilibria. 1. united-atom description of n-alkanes. *The Journal of Physical Chemistry B* **102**, 2569–2577 (1998).
66. Van Gunsteren, W. F. & Berendsen, H. J. A leap-frog algorithm for stochastic dynamics. *Molecular Simulation* **1**, 173–185 (1988).
67. Hess, B., Bekker, H., Berendsen, H. J. & Fraaije, J. G. Lincs: a linear constraint solver for molecular simulations. *Journal of computational chemistry* **18**, 1463–1472 (1997).
68. Sedghi, M. *et al.* Molecular dynamics simulations of asphaltene dispersion by limonene and pvac polymer during Co<sub>2</sub> flooding. In *SPE International Conference and Exhibition on Formation Damage Control* (Society of Petroleum Engineers, 2016).
69. Qian, J.-W., Jaubert, J.-N. & Privat, R. Prediction of the phase behavior of alkene-containing binary systems with the ppr78 model. *Fluid Phase Equilibria* **354**, 212–235 (2013).
70. Davis, H. & Scriven, L. Stress and structure in uid interfaces. *Adv. Chem. Phys* **49**, 357–454 (1982).
71. Davis, H. T. *Statistical mechanics of phases, interfaces, and thin films* (VCH New York, 1996).
72. Nist chemistry webbook, nist standard reference database number 69, <http://webbook.nist.gov/>.

## Acknowledgements

This publication is partly based upon work supported by the KAUST Office of Sponsored Research (OSR) under Award No. 2993. N.C., M.F.A.C.R., and A.K.N.N. would like to thank computational support from KAUST.

## Author contributions

A.K.N.N. and S.S. conceived the project. A.K.N.N. designed the project and wrote the paper. N.C. and M.F.A.C.R. conducted the simulations and theoretical modeling, respectively. All authors reviewed the manuscript.

## Competing interests

The authors declare no competing interests.

## Additional information

**Correspondence** and requests for materials should be addressed to A.K.N.N. or S.S.

**Reprints and permissions information** is available at [www.nature.com/reprints](http://www.nature.com/reprints).

**Publisher's note** Springer Nature remains neutral with regard to jurisdictional claims in published maps and institutional affiliations.



**Open Access** This article is licensed under a Creative Commons Attribution 4.0 International License, which permits use, sharing, adaptation, distribution and reproduction in any medium or format, as long as you give appropriate credit to the original author(s) and the source, provide a link to the Creative Commons license, and indicate if changes were made. The images or other third party material in this article are included in the article's Creative Commons license, unless indicated otherwise in a credit line to the material. If material is not included in the article's Creative Commons license and your intended use is not permitted by statutory regulation or exceeds the permitted use, you will need to obtain permission directly from the copyright holder. To view a copy of this license, visit <http://creativecommons.org/licenses/by/4.0/>.

© The Author(s) 2019